Nonlinear waves in the pressure driven flow in a finite rotating pipe

E. Sanmiguel-Rojas
Universidad Politécnica de Cartagena, Escuela Técnica Superior de Ingenieros Industriales, 30202 Cartagena, Murcia, Spain

R. Fernandez-Feria
Universidad de Málaga, Escuela Técnica Superior de Ingenieros Industriales, 29013 Málaga, Spain

(Received 25 June 2004; accepted 5 October 2004; published online 9 December 2004)

To investigate the nature of nonlinear waves appearing in an axially rotating pipe, we have performed a series of time-depending, three-dimensional numerical simulations of the incompressible Navier–Stokes equations in a rotating long pipe. As a difference with some previous works on the subject, which look for several given types of traveling wave solutions in pipes of infinite length, we leave the flow to evolve freely after a pressure difference is set between two points, one on each end of the finite rotating pipe. We use a recently developed numerical method that allows us to simulate numerically the three-dimensional flow produced in a pipe when Dirichlet boundary condition for the pressure is given on part of the inlet and outlet sections of the pipe. This technique is further improved here so that the pressure is only fixed at just one point on each one of the open boundaries of the pipe. Thus, no restrictions on the flow properties are given in these sections, allowing the free entrance and exit of possible waves through the pipe. We find that packets of traveling spiral waves are formed for values of the Reynolds numbers based on both the axial and the azimuthal velocities just above the critical ones given by the linear stability theory. These traveling waves have the same characteristics predicted by the linear stability theory and produce no significant mean flux defect. As the values of these parameters are increased above their critical values, the spiral waves become more involved and their amplitude increase, giving rise to a significant axial mean flow defect. For sufficiently high Reynolds numbers, we detect the apparition of spiral waves traveling also upstream, in agreement with the stability analysis for absolute instabilities. At the end, these traveling waves appearing above the onset for absolute instabilities transform into a standing spiral wave superimposed to the rotating Hagen–Poiseuille flow. © *2005 American Institute of Physics*. [DOI: 10.1063/1.1828124]

I. INTRODUCTION

The linear stability of rotating Hagen–Poiseuille flow (RHPF) is a well studied problem. Contrary to nonrotating Hagen–Poiseuille flow, which is well known to be linearly stable for all Reynolds number, it was first shown by Pedley[1] that RHPF becomes linearly unstable for finite Reynolds numbers if the rotation of the pipe about its axis is high enough. The stability properties of this flow in terms of the axial flow Reynolds number and the Reynolds number based on the angular velocity of rotation (Re_Q and Re_θ, two parameters that will be defined below) were fully characterized by Mackrodt[2] and by Cotton and Salwen,[3] among others. More recently, the onset of absolute instabilities in RHPF has been also characterized.[4] These stability analyses predict the formation of traveling nonaxisymmetric (spiral) waves, whose nonlinear structure and stability have been further considered.[5,6]

The objective of this work is to perform a series of numerical simulations (numerical experiments) in a long, but of course finite, rotating pipe which may shed some new light on the formation, evolution, and structure of these nonlinear traveling waves that are formed after instability of RHPF. In particular, we are curious about the nature of the flow after the onset of absolute instability. It has been postulated that absolute instability may be the precursor of vortex breakdown in some swirling jets.[7,8] This connection has not been assessed numerically due, mainly, to the difficulties in the numerical simulation of general three-dimensional (3D) and incompressible open jets and wakes. However, these difficulties can be circumvented in a three-dimensional flow confined in a pipe, even if one considers open inlet and outlet boundaries that do not constrain the movement of traveling waves through them. To that end we use here a recently developed numerical technique for incompressible flows[9] in which a pressure difference between the inlet and outlet sections of the pipe is set at the start and then the flow is left to evolve freely in time. This configuration is easily realized in the laboratory (for instance, a pipe discharging from a large container to the atmosphere). Numerically, the pressure is specified directly only at closed curves on the inflow and outflow surfaces, so that the desired pressure difference is enforced in the pipe without constraining the flow on the open boundaries. We have developed further that technique here (see the Appendix for a summary), so that one only needs to fix the pressure at just one point on each open boundary. In these open boundaries, the velocity field and the pressure are left to evolve freely in time according to the Navier–Stokes equation and the incompressibility constraint, except for the pressure at the two points where the pressure

is given, so that one may account for the inflow and outflow of any traveling wave. With this tool, we have performed a series of numerical experiments for several representative cases of Re_Q and Re_θ, which have been selected according to the known results on the linear stability of RHPF.

II. FORMULATION OF THE PROBLEM

We consider here the incompressible flow in a pipe of radius R and length $l \times R$ driven by a pressure difference Δp_c. The pipe rotates at an angular velocity Ω around its axis of symmetry. The nondimensional Navier–Stokes equations governing the flow can be written as

$$\boldsymbol{\nabla} \cdot \mathbf{v} = 0, \tag{1}$$

$$\frac{\partial \mathbf{v}}{\partial t} + \mathbf{v} \cdot \boldsymbol{\nabla}\, \mathbf{v} = - \boldsymbol{\nabla}\, p + \frac{1}{\mathrm{Re}} \nabla^2 \mathbf{v}, \tag{2}$$

where $\mathbf{v}$ and p are the dimensionless velocity and pressure, respectively. The pressure also includes, as usual, any volume force that can be written in gradient form (such as gravity). We use cylindrical-polar coordinates (r, θ, x) with the coordinate x along the axis of the pipe, and the velocity components $\mathbf{v} \equiv (u, v, w)$. To nondimensionalize the geometry and the flow magnitudes we use the pipe radius R as the length scale and a characteristic velocity based on the pressure difference $V_c = \sqrt{\Delta p_c / \rho}$, where ρ is the fluid density. Accordingly, the Reynolds number in (2) is

$$\mathrm{Re} = \frac{V_c R}{\nu} = \sqrt{\frac{\Delta p_c}{\rho}} \frac{R}{\nu}, \tag{3}$$

with ν being the kinematic viscosity.

We want to solve Eqs. (1) and (2) subjected to the boundary conditions that the velocity on the pipe wall is given by

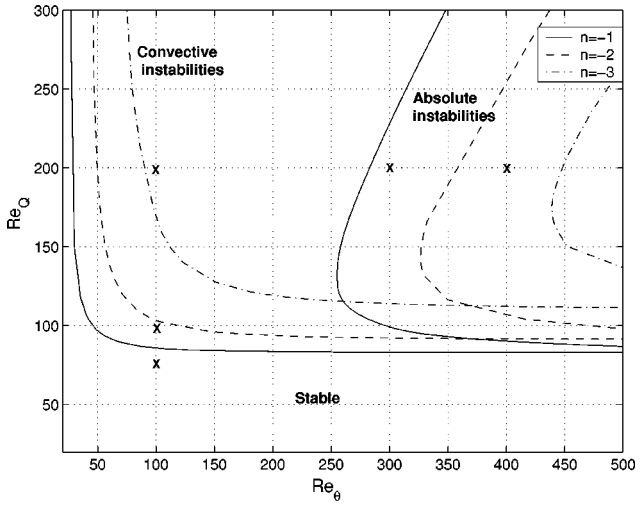

FIG. 1. Values of Re_Q and Re_θ for the different numerical simulations considered (crosses) on a stability diagram. The lines represent the neutral curves for convective and absolute instabilities for different values of the azimuthal wave number n. The neutral curve for convective instability ($n = -1$) was first obtained by Mackrodt (Ref. 2). All the curves are taken from Ref. 4.

$$u = w = 0, \quad v = \frac{\Omega R}{V_c} \text{ for } r = 1, \quad 0 \leqslant x \leqslant l, \tag{4}$$

and the pressure p is given at two points, one on the inflow surface and the other one at the outflow surface,

$$p = 1 \text{ at } x = 0, \quad r = 0 \tag{5a}$$

and

$$p = 0 \text{ at } x = l, \quad r = 0, \tag{5b}$$

so that a dimensional pressure difference Δp_c is set between the pipe ends. The inlet and outlet pressure distributions, $p_i(r, \theta, t)$ and $p_o(r, \theta, t)$, are obtained as part of the solution using a slightly modified version of the numerical method developed in Ref. 9, which is summarized in the Appendix.

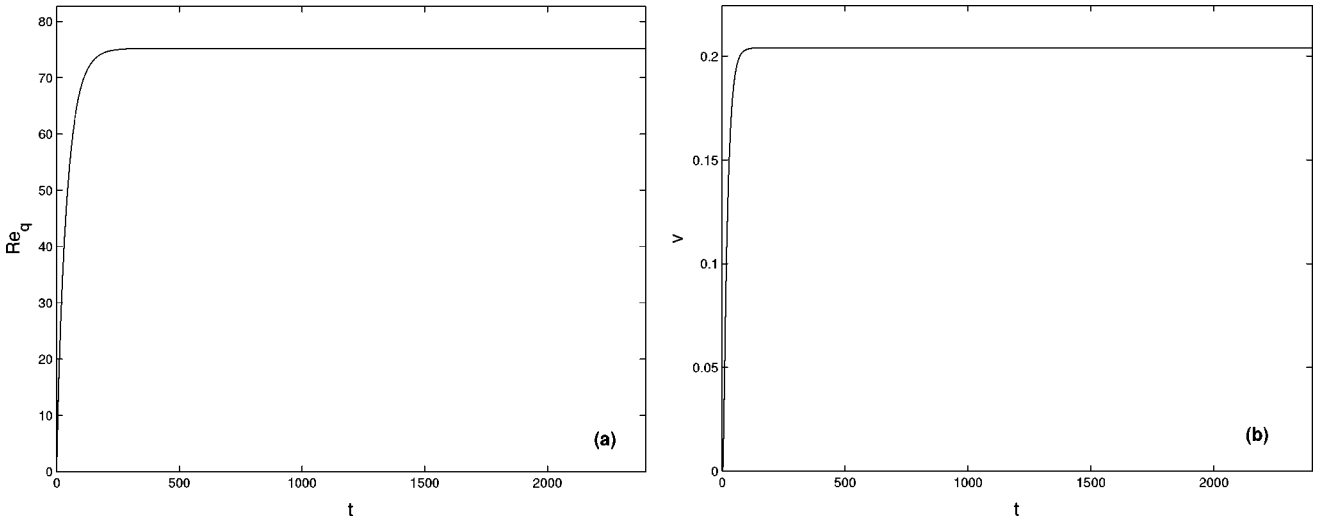

FIG. 2. (a) $\mathrm{Re}_q(t)$ for $\mathrm{Re}_Q = 75$ and $\mathrm{Re}_\theta = 100$. (b) Time evolution of the azimuthal velocity v at $r = 1/2$, $\theta = 0$, and $x = 100$.

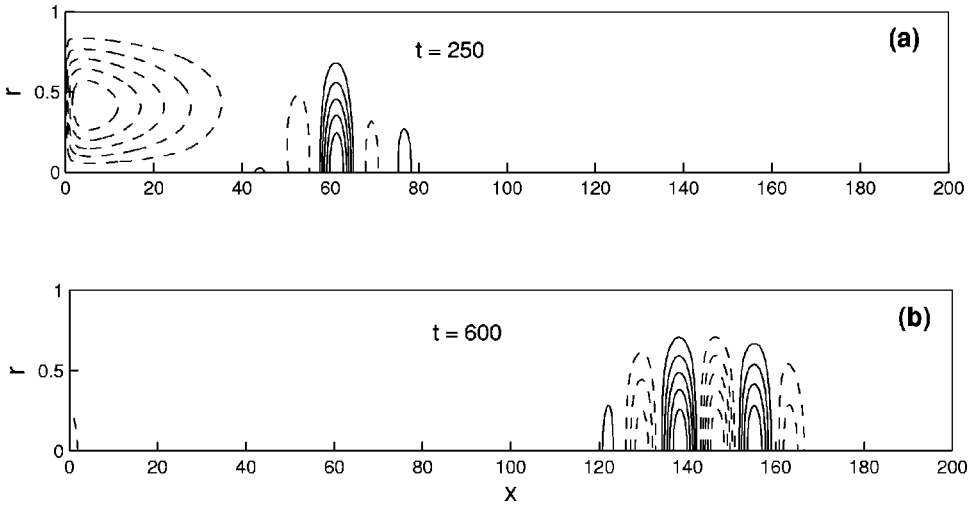

FIG. 3. Contour lines of the radial velocity u on the rx plane for $\theta=0$ and for two different instants of time (as indicated) in the case $\mathrm{Re}_Q=75$ and $\mathrm{Re}_\theta=100$. Continuous (dashed) lines correspond to positive (negative) values of u. Five equidistant contour lines of u in each one of the intervals $[-4.46\times10^{-11},0]$ and $[0,1.67\times10^{-11}]$ are plotted in (a), and in the intervals $[-4.79\times10^{-13},0]$ and $[0,4.39\times10^{-13}]$ in (b).

As the initial condition we suppose the fluid is at rest and there is a linear distribution of p between $x=0$ and $x=1$.

To relate the Reynolds number (3) to the usual pipe Reynolds number based on the mean axial flow rate, we compute the instantaneous flow rate $q(t)$ at the outflow section,

$$\mathrm{Re}_q(t)=\mathrm{Re}\,\frac{1}{\pi}\int_0^{2\pi}\int_0^1 (rw)_{x=l}\,d\theta\,dr. \tag{6}$$

For a Hagen–Poiseuille flow, $\lim_{t\to\infty}\mathrm{Re}_q\to\mathrm{Re}_Q$, which is related to Re through

$$\mathrm{Re}=\sqrt{4l\,\mathrm{Re}_Q}. \tag{7}$$

For a long rotating pipe, we shall see that Re_q will tend to Re_Q, except if a strong nonlinear wave is developed inside the flow that produces a significant axial mean flow defect.

The flow is characterized by, in addition to the nondimensional pipe length l, two Reynolds numbers Re_Q (or Re) and a Reynolds number based on the angular rotation of the pipe

$$\mathrm{Re}_\theta\equiv\frac{\Omega R^2}{\nu}. \tag{8}$$

Alternatively, one might use a swirl parameter $L\equiv\mathrm{Re}_\theta/\mathrm{Re}_Q$ instead of Re_θ. In terms of these nondimensional parameters, the boundary condition (4) for v may be written as

$$v=\mathrm{Re}_\theta/\mathrm{Re}\ \text{at}\ r=1. \tag{9}$$

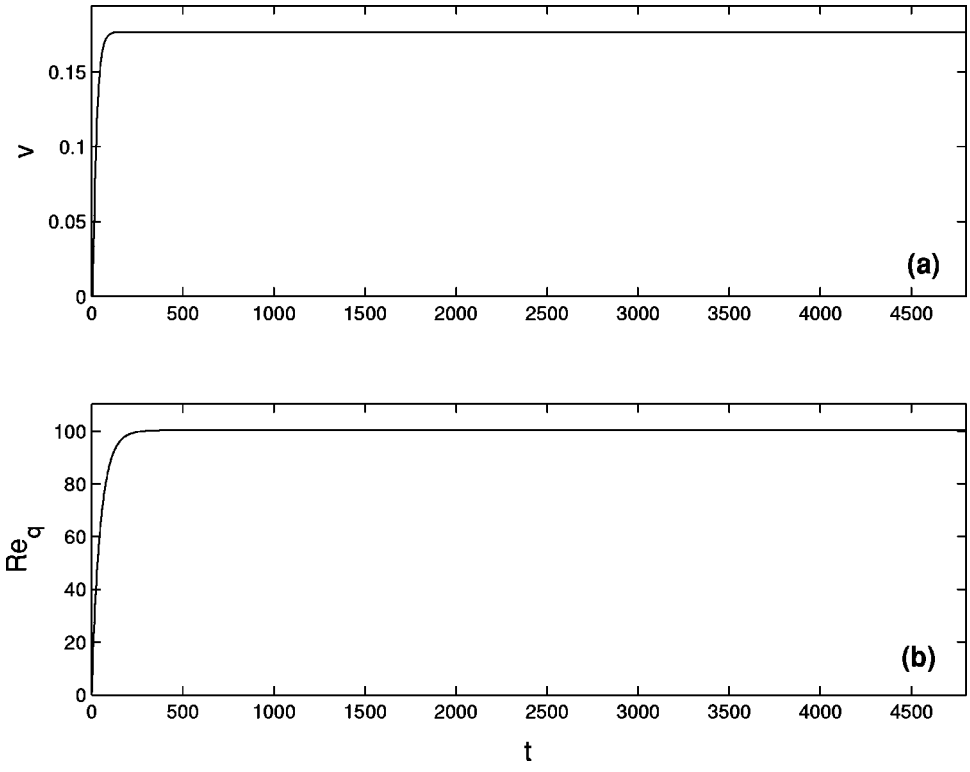

FIG. 4. (a) Time evolution of the azimuthal velocity v at $r=1/2$, $\theta=0$, and $x=100$ for $\mathrm{Re}_Q=100$ and $\mathrm{Re}_\theta=100$. (b) $\mathrm{Re}_q(t)$ for the same case.

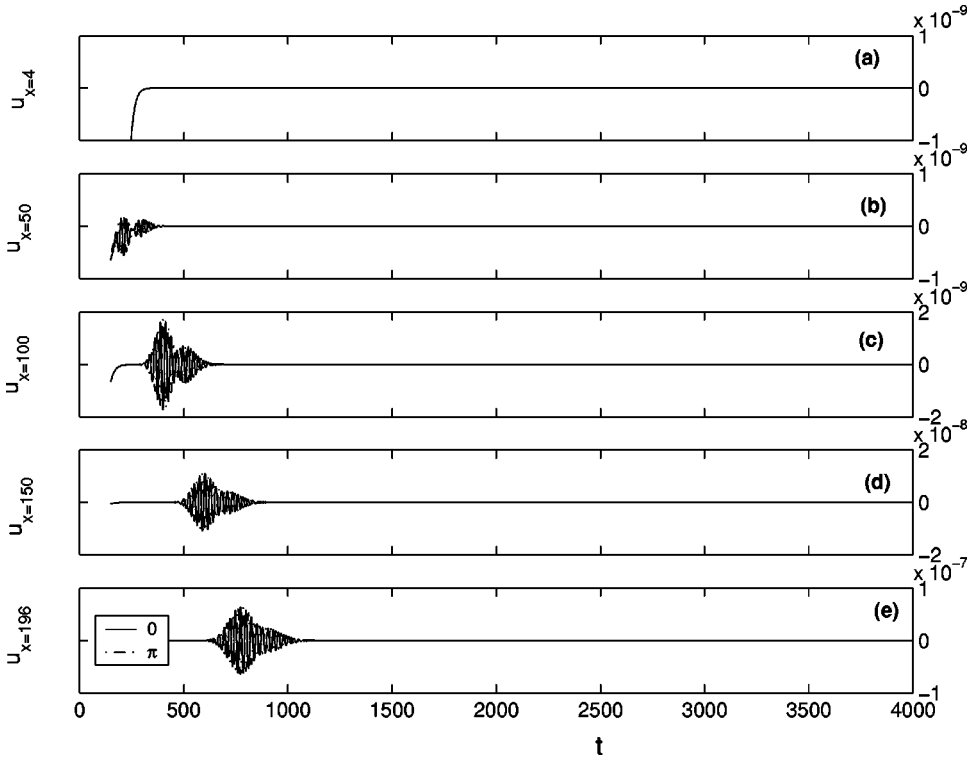

FIG. 5. Time evolution of the radial velocity u at $r=1/2$, $\theta=0$ (solid lines) and $\theta=\pi$ (dashed lines), and five axial location (two diameters after the pipe inlet, $1/4$ of the pipe length, half the pipe length, $3/4$ of the pipe length, and 2 diameters before the exit) for $\mathrm{Re}_Q=100$ and $\mathrm{Re}_\theta=100$.

III. RESULTS

In this section we present the results from several numerical simulations for different values of Re_Q and Re_θ. As shown in Fig. 1, these values have been selected to cover the main transitions predicted by the linear stability analysis of RHPF. In all the cases we have used a pipe of length $l=200$. All the numerical simulations started with the fluid at rest and the pipe rotating at the angular velocity corresponding to Re_θ. As time goes on, the flow acquires the corresponding solid body rotation rather quickly, and the nominal axial flow rate Re_Q is reached typically after several hundred of nondimensional time units (see below). The different numerical parameters used in the simulations are given in the Appendix. We have chosen to start the simulations with the fluid at rest because we believe that it is the most relevant initial condition from a physical point of view and because it is simpler to implement numerically. Any other initial condition for the velocity field would require the computation of a nontrivial initial pressure distribution different from the axially linear one [an initial pressure distribution is needed to start the computations owing to the alternate direction implicit (ADI) technique we use to solve the Poisson equation for the pressure; see the Appendix].

A. $\mathrm{Re}_Q=75$, $\mathrm{Re}_\theta=100$

As seen in Fig. 1, this case corresponds to a linearly stable flow. Figure 2 shows that the nominal Reynolds number $\mathrm{Re}_Q=75$ is reached at $t\sim250$, while the solid body rotation at the center of the pipe is reached more quickly, at about half of that time. The numerical simulations show that, in effect, the asymptotic Hagen–Poiseuille flow with superimposed solid body rotation is stable. Actually, the simulations show that very small perturbations, with amplitude in terms of the radial velocity $|u|\sim10^{-11}$, are generated near the inlet due to numerical noise, but these infinitesimal waves decay as they propagate along the pipe, exiting it with an amplitude of order 10^{-13} (see Fig. 3).

B. $\mathrm{Re}_Q=100$, $\mathrm{Re}_\theta=100$

This case, which corresponds to $\mathrm{Re}\simeq282.64$, lies just above the critical conditions for convective instability (see Fig. 1). The time evolution of Re_q and the azimuthal velocity v at the center of the pipe are plotted in Fig. 4. It is observed that the nominal flow rate $\mathrm{Re}_Q=100$ is reached at $t\sim250$, while the solid body rotation is reached at $t\sim125$. This initial transient behavior remains approximately valid for all the cases considered. The radial velocity u at $r=1/2$ and several axial locations for $\theta=0$ and $\theta=\pi$ are plotted in Fig. 5. As in the above case, we have selected the radial velocity to detect the perturbations because $u=0$ for the unperturbed flow. This figure shows that a nonaxisymmetric perturbation is formed near the pipe inlet at about the time Re_q reaches its asymptotic value. The amplitude of this wave grows more

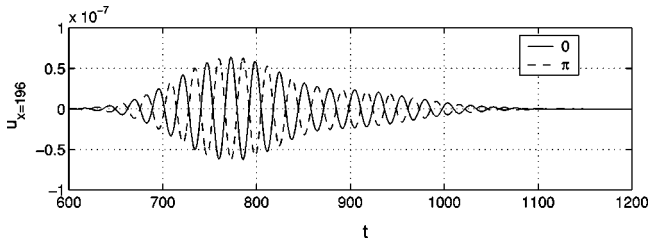

FIG. 6. Detail of the time evolution of the radial velocity at the last axial location plotted in Fig. 5.

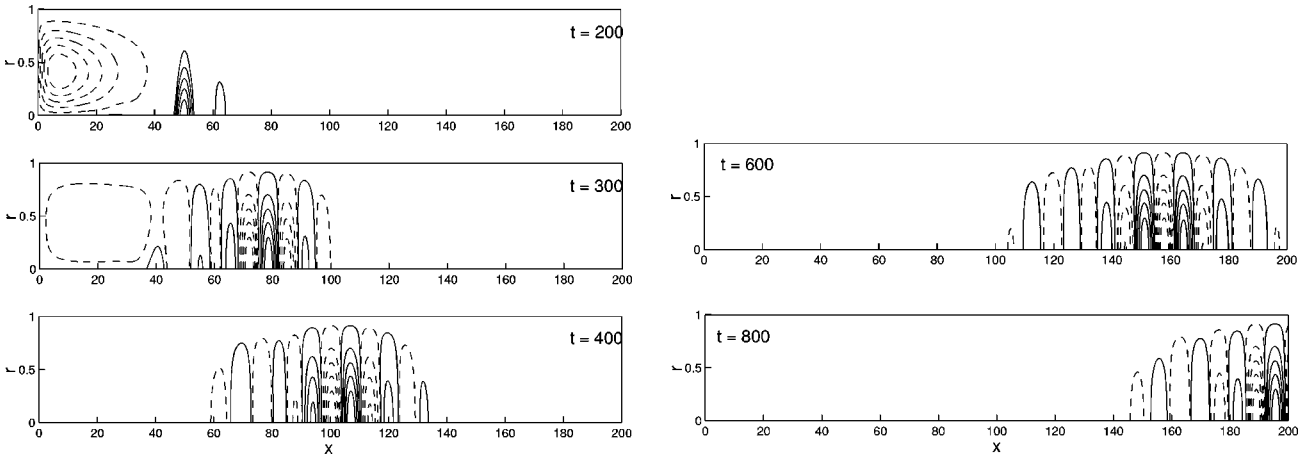

FIG. 7. Contour lines of the radial velocity u on the rx plane for $\theta=0$ and for different times (as indicated) in the case $\mathrm{Re}_Q=100$ and $\mathrm{Re}_\theta=100$. Continuous (dashed) lines correspond to positive (negative) values of u. Five positive and five negative equidistant contour lines of u are plotted in the following intervals: $[-1.25\times10^{-8},6.95\times10^{-10}]$ for $t=200$, $[-1.24\times10^{-9},1.40\times10^{-9}]$ for $t=300$, $[-3.39\times10^{-9},3.31\times10^{-9}]$ for $t=400$, $[-2.50\times10^{-8},2.25\times10^{-8}]$ for $t=600$, and $[-6.36\times10^{-8},1.09\times10^{-7}]$ for $t=800$.

than two orders of magnitude as it travels along the pipe, leaving the flow unperturbed behind (see also Figs. 7 and 8 below). This is what is expected in a convective instability. From this figure, the group velocity of this traveling wave packet is $c_g\simeq0.255$. A detailed view of this wave packet in the last axial location plotted in Fig. 5 is shown in Fig. 6, from where one may compute the period T and the frequency of the waves $\omega=2\pi/T\simeq0.245$.

The wavelength of these waves may be computed from the contour lines on the rx plane of the radial velocity, shown in Fig. 7 at several instants of time for $\theta=0$. One observes that the perturbation originates near the pipe inlet ($x\sim50$) at the vicinity of the axis of symmetry. Then the wave packet travels downstream, increasing their amplitude by more than two orders of magnitude when it exits the pipe (it is seen that, with the present numerical technique, there is no restriction on the form of the flow exiting the pipe). From this figure, the wavelength is $\lambda\simeq13.5$, which corresponds to an axial wave number $\alpha=2\pi/\lambda\simeq0.465$. Finally, to find out the azimuthal wave number n one may use the contour lines of u in the θx plane, shown in Fig. 8 at several instants of time and $r=1/2$. Taking into account that the phase of the wave for a given t is constant in that plane when $n\theta+\alpha x$ is constant, and using the value of α computed above, one finds that $n\simeq-1$. [That $|n|=1$ is clear from the fact that $u\neq0$ in Fig. 7 at the axis of symmetry $r=0$ (Ref. 10)]. This is further corroborated in Fig. 9, which depicts the contour lines of u at the pipe exit. This figure shows that $|n|=1$ and that the perturbations are concentrated at the axis of symmetry. All the above values of the traveling waves properties found numerically agree with the ones obtained from the stability analysis corresponding to the most unstable mode in the rotating Hagen–Poiseuille flow for $\mathrm{Re}_Q=100$ and $\mathrm{Re}_\theta=100$, which are[4] $n=-1$, $\alpha\simeq0.432$, $\omega\simeq0.251$, and $c_g\simeq0.258$. (It has been taken into account that the characteristic time used in the cited stability analysis is $\mathrm{Re}/\mathrm{Re}_Q\simeq2.828$ times the characteristic time used in this work.)

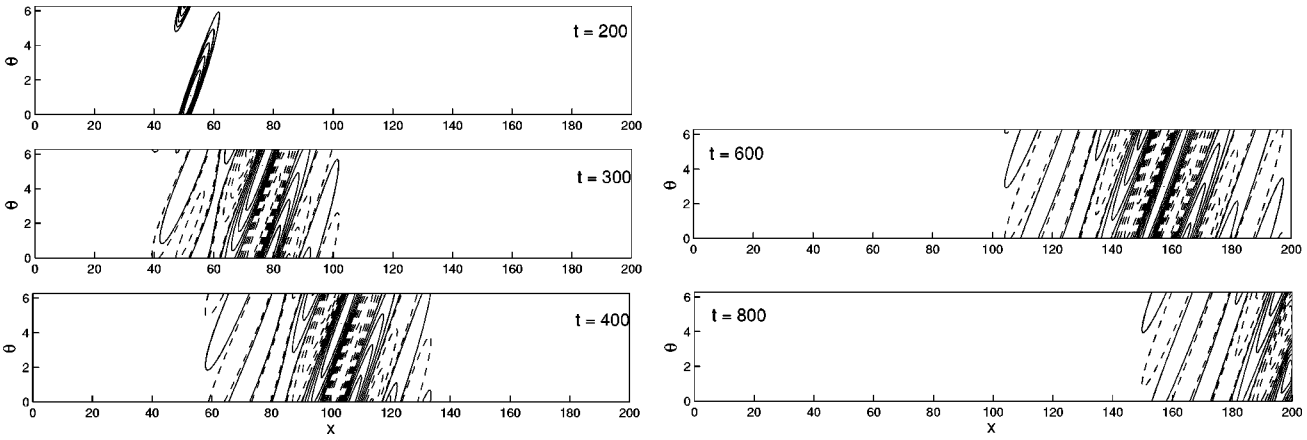

FIG. 8. Contour lines of the radial velocity u on the θx plane for $r=1/2$ and for different instants of time (as indicated) in the case $\mathrm{Re}_Q=100$ and $\mathrm{Re}_\theta=100$. Continuous (dashed) lines correspond to positive (negative) values of u. Five positive and five negative equidistant isocontours of u are plotted in the following intervals: $[0,1.70\times10^{-10}]$ for $t=200$, $[-7.36\times10^{-10},7.30\times10^{-10}]$ for $t=300$, $[-1.81\times10^{-9},1.81\times10^{-9}]$ for $t=400$, $[-1.29\times10^{-8},1.28\times10^{-8}]$ for $t=600$, and $[-7.40\times10^{-8},7.40\times10^{-7}]$ for $t=800$.

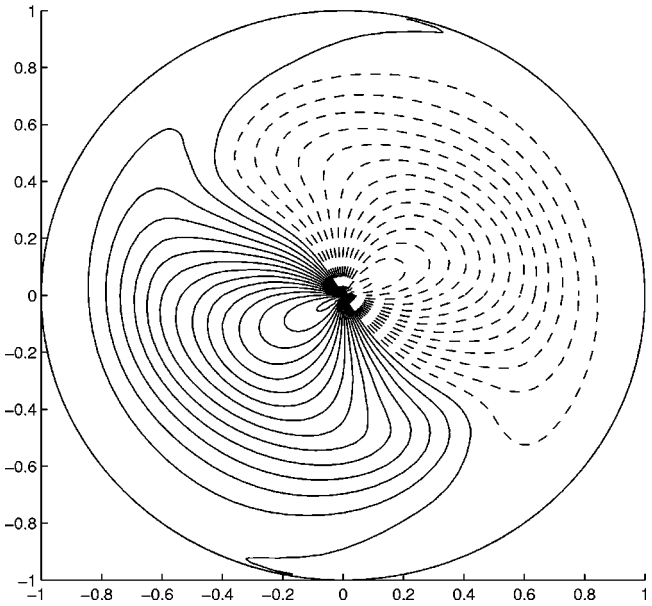

FIG. 9. Contour lines of the radial velocity u on the θr plane at the pipe exit ($x=200$) and $t=4800$ for $\mathrm{Re}_Q=100$ and $\mathrm{Re}_\theta=100$. Continuous (dashed) lines correspond to positive (negative) values of u.

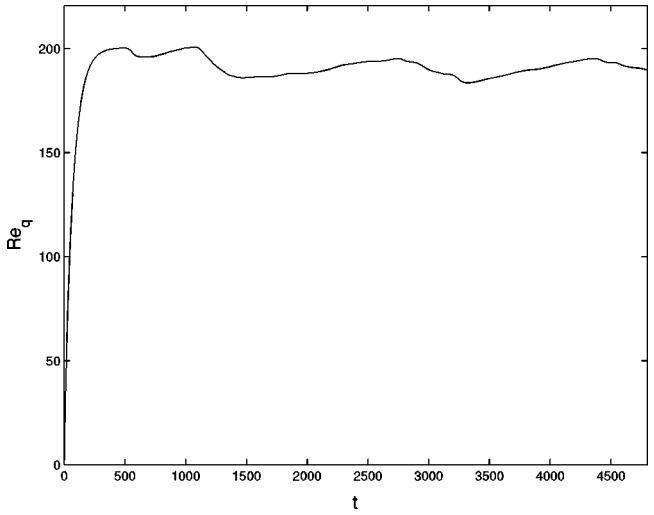

FIG. 10. $\mathrm{Re}_q(t)$ for $\mathrm{Re}_Q=200$ and $\mathrm{Re}_\theta=100$.

C. $\mathrm{Re}_Q=200$, $\mathrm{Re}_\theta=100$

This case is well inside the convective instability region of the rotating Hagen–Poiseuille flow (see Fig. 1), and corresponds to $\mathrm{Re}=400$. The unstable perturbations do not remain small along the pipe as in the above case, but their amplitudes grow to become important fractions of the unperturbed mean flow. As a consequence, a significant axial mean flow defect is produced when the instability is developed in the flow. This is shown in Fig. 10, where one observes that once the nominal flow rate $\mathrm{Re}_Q=200$ is approximately reached at about $t=300$, the flow rate decreases due to the fact that a significant part of the energy put into the system as a pressure difference is *wasted* in the finite amplitude waves produced by the unstable perturbations. That the flow no longer corresponds to a RHPF is clearly seen in Fig. 11.

The oscillatory behavior of $\mathrm{Re}_q(t)$ observed in Fig. 10 is due to the passing of the successive finite amplitude wave packets along the pipe (see Figs. 12–14), showing that the instability is still convective, as predicted by the stability analysis for these values of the Reynolds numbers. (In the previous case the behavior is qualitatively the same, but the oscillations are not observed in Fig. 4 because the amplitude of the waves remains infinitesimal, and so does the mean flow defect.) The first thing one may observe in Fig. 13 is that the instability is produced near the axis of the pipe at $x\sim 50$, at about $t\simeq 250$, approximately when the nominal Reynolds number $\mathrm{Re}_Q=200$ is reached (Fig. 10). According to this figure, the amplitude of the perturbations grows more than five orders of magnitude as the wave travels along the pipe [from $O(10^{-7})$ to $O(10^{-2})$]. Just when this first wave packet is exiting the pipe at $t\sim 600$, the mean flow rate computed on this section is lower (Fig. 10). After the formation

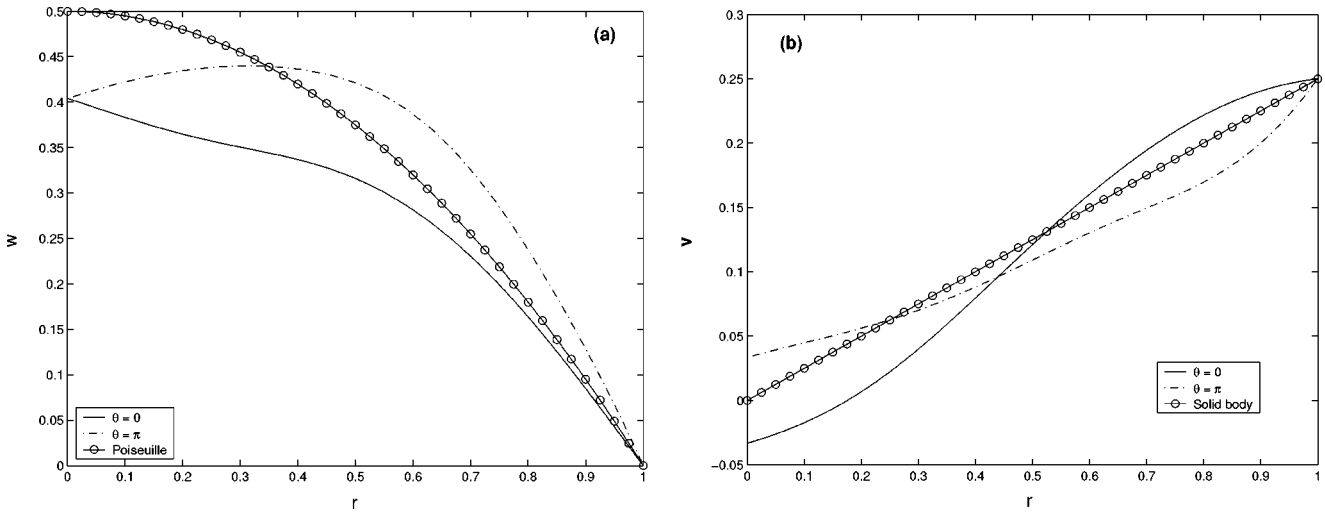

FIG. 11. Radial profiles of the axial velocity (a) and the azimuthal velocity (b) for $\mathrm{Re}_Q=200$ and $\mathrm{Re}_\theta=100$ at the pipe exit ($x=200$), for $\theta=0$ (continuous lines) and $\theta=\pi$ (dash and dot lines). Also shown (circles) are the parabolic Hagen–Poiseuille axial velocity (a) and the linear azimuthal velocity for a solid body rotation (b).

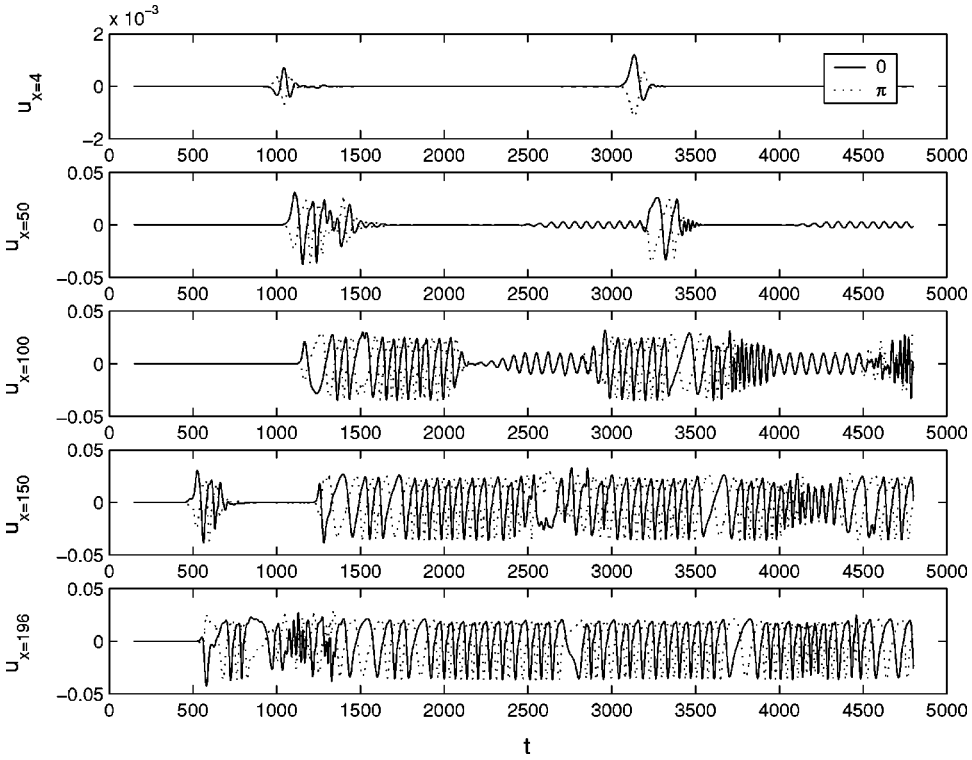

FIG. 12. As in Fig. 5 but for $\mathrm{Re}_Q=200$ and $\mathrm{Re}_\theta=100$.

of this first wave packet, successive wavetrains of finite amplitude are originated at approximately the same axial location and travel along the pipe, producing the oscillatory pattern in the mean flow rate. Thus, at $t=1200$, one sees in Fig. 14 that a second wave packet has developed before the first one has exited the pipe. For later times, this figure shows an almost continuous wavetrain. Although the characteristics of these spiral wavetrains are not completely uniform in the axial direction as the different waves evolve along the pipe (see also Fig. 15, where a 3D view of the waves is given for the last time of the computations), they share in common that the azimuthal wave number is always $n=-1$, as indicated by the fact that the radial velocity in Figs. 13 and 14 does not vanish at the axis $r=0$. This is further corroborated in Fig. 16, which depicts the contour lines of u at the pipe exit for the last computation time. That $n=-1$ agrees with the stability analysis, for though Fig. 1 shows that modes with $n=-1,-2$, and -3 are unstable for the present values of Re_Q and Re_θ, $n=-1$ is the first mode to become unstable for $\mathrm{Re}_\theta=100$ as Re_q increases, and remains the most unstable one for $\mathrm{Re}_Q=200$.[4]

D. $\mathrm{Re}_Q=200$, $\mathrm{Re}_\theta=300$

We now increase the angular velocity of the rotating pipe to $\mathrm{Re}_\theta=300$ maintaining the same pressure difference of the

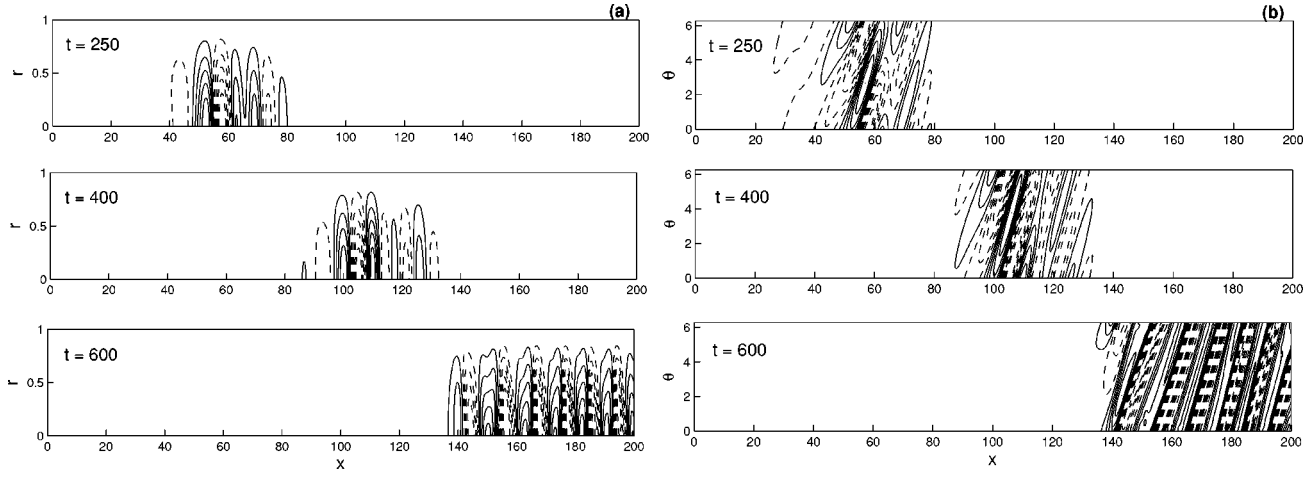

FIG. 13. Contour lines of the radial velocity u at $\theta=0$ on the rx plane (a) and for $r=1/2$ on the θx-plane (b) for different times (as indicated) in the case $\mathrm{Re}_Q=200$ and $\mathrm{Re}_\theta=100$. Continuous (dashed) lines correspond to positive (negative) values of u. Nine positive and nine negative equidistant contour lines of u are plotted in the following intervals: (a) $[-9\times10^{-7},6.1\times10^{-7}]$ for $t=250$, $[-4.4\times10^{-4},3.5\times10^{-4}]$ for $t=400$, and $]-0.05,0.05]$ for $t=600$; (b) $[-5.0\times10^{-7},4.7\times10^{-7}]$ for $t=250$, $[-2.4\times10^{-4},2.4\times10^{-4}]$ for $t=400$, and $[-0.039,0.026]$ for $t=600$.

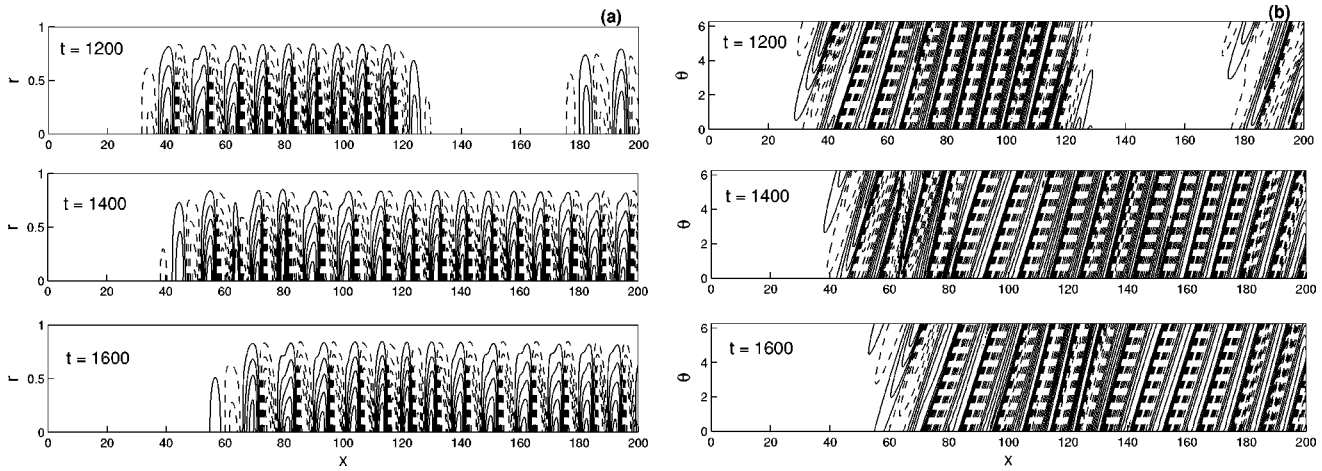

FIG. 14. As in Fig. 13, but for different times (as indicated). The range of values of u plotted are the following: (a) $[-0.057, 0.057]$ for $t=1200$, $[-0.052, 0.049]$ for $t=1400$, and $[-0.05, 0.05]$ for $t=1600$; (b) $[-0.038, 0.034]$ for $t=1200$, $[-0.036, 0.032]$ for $t=1400$, and $[-0.036, 0.031]$ for $t=1600$.

above case ($\mathrm{Re}=400$), and thus the nominal flow rate $\mathrm{Re}_Q=200$. As seen in Fig. 1, this case is just inside the region of absolute instability, a fact that, as we shall see, introduces a qualitative change in the behavior of the flow. As in the previous case, the formation of waves of finite amplitude after the instability of the RHPF produces a significant mean flow defect. However, as a difference with the previous case, we see in Fig. 17 that a steady state is reached after decreasing the mean flow rate from the nominal value, instead of the oscillatory behavior observed in Fig. 10.

What happens is that the spiral waves formed after the instability of RHPF not only travel downstream as in the previous cases, but at some instant they begin to travel also upstream, modifying the whole flow pattern until a new nonaxisymmetric flow, with a standing wave superimposed to the original RHPF and with constant mean flow rate, is reached. This set of events can be observed in the Figs. 18–20. A convective instability is first formed at $x\sim 40$, and at about the same time ($t\sim 250$) the nominal Reynolds number $\mathrm{Re}_Q=200$ is reached (Fig. 18). The amplitude of the wave thus formed, which has an azimuthal wave number $n=-1$ (note that $u\neq 0$ at the axis), grows very rapidly as it travels downstream. Eventually, this wave also evolves upstream, becoming more complex and intense all along the pipe (Fig. 18 at $t=600$). At $t\simeq 800$, waves with a different azimuthal wave number $n=-2$ (note that $u=0$ at the axis) are also formed at this new axial location nearer the pipe inlet and propagate downstream replacing the former wavetrain with $n=-1$ (Fig. 19). At $t\sim 1600$, a new wavetrain with again $n=-1$ is formed near the pipe inlet, mixing with the former one with $n=-2$ (Fig. 20). This wave also propagates further upstream, till a standing (steady state) wave with a complex pattern, superposition of modes with $n=-1$ and $n=-2$ (see also Fig. 21), is set all along the pipe. Thus, for this Reynolds number, the absolute instability marks the onset of the formation of a complex standing wave. Figure 20 shows that the wavelength of this standing wave is $\lambda\simeq 26$ (axial wave number $\alpha\simeq 0.24$).

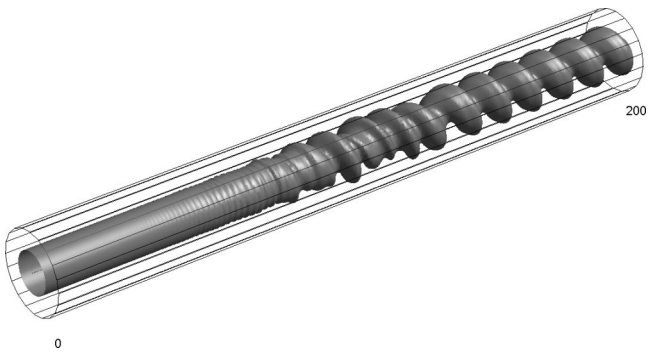

FIG. 15. 3D view of the isosurface $w=0.35$ for $t=4800$ in the case $\mathrm{Re}_Q=200$ and $\mathrm{Re}_\theta=100$.

E. $\mathrm{Re}_Q=200$, $\mathrm{Re}_\theta=400$

We now increase further the angular velocity of rotation to $\mathrm{Re}_\theta=400$ for the same pressure difference. The evolution of the flow is qualitatively similar to that of the previous case (Fig. 22). A convective instability with $n=-1$ is first formed at $x\sim 40$ for $t\sim 250$. The amplitude of this wave increase as it propagates downstream. It also propagates upstream (absolute instability). Then, a second perturbation with $n=-2$ grows as it pervades the pipe. But, as a difference with the previous case, this wave with $n=-2$ is the one that becomes the final standing wave (note in Fig. 22 that the steady state in this case is reached faster than in Fig. 17). The final steady state is shown in Figs. 23 and 24. The axial wavelength of the wave with $n=-2$ is $\lambda\simeq 19$ ($\alpha\simeq 0.33$).

IV. SUMMARY AND CONCLUSIONS

We have performed in this work a series of three-dimensional numerical simulations of the incompressible flow driven by a pressure difference in a rotating pipe of length 200 times its radius. We have used a recently developed numerical technique that allows us to simulate the incompressible flow when the pressure is fixed at just two points, one on each end of the pipe, so that the flow evolves freely in time, allowing the formation and evolution of possible nonlinear waves, including the open end sections. For a

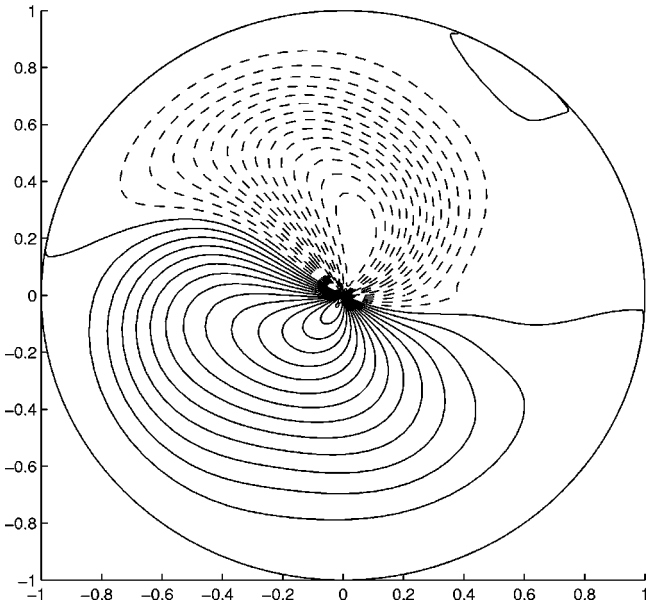

FIG. 16. As in Fig. 9, but for $\mathrm{Re}_Q=200$. Fifteen equidistant contour lines of u are plotted in the intervals $[-0.04,0]$ and $[0,0.038]$.

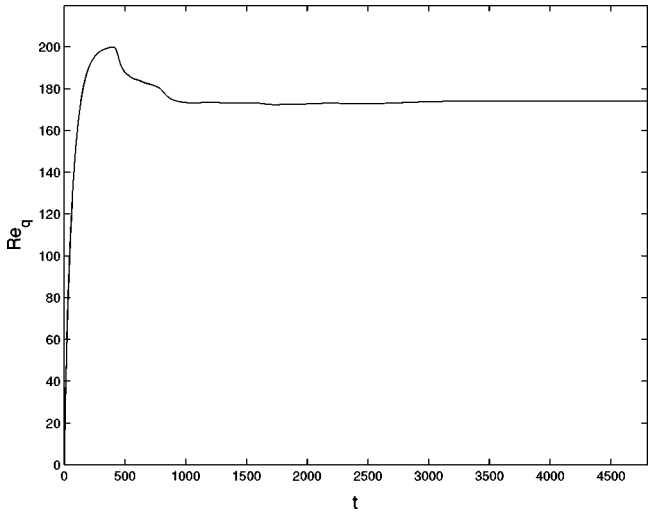

FIG. 17. $\mathrm{Re}_q(t)$ for $\mathrm{Re}_Q=200$ and $\mathrm{Re}_\theta=300$.

given rotation rate ($\mathrm{Re}_\theta=100$), we have first considered two axial Reynolds numbers close to the neutral curve for linear stability of the RHPF, one on each side of the curve ($\mathrm{Re}_Q=75$ and $\mathrm{Re}_Q=100$). For the stable case we observe that all the infinitesimal waves formed from the numerical noise are rapidly damped as they travel downstream, while in the unstable case we show that the amplitude of some waves grow as they travel downstream the pipe. In particular, we observe that these unstable wave packets are spiral waves with an azimuthal wave number $n=-1$, and their properties (axial wavelength, frequency, and group velocity) coincide with the values given by the linear stability analysis. Thus we show that the numerical technique correctly simulates the onset of convective instabilities.

Although for $\mathrm{Re}_Q=100$ the amplitude of the wave packets grows downstream, as predicted by the linear stability analysis, their intensities remain infinitesimal all along the pipe because this case is very close to the neutral stability curve (see Fig. 1). Consequently, no appreciable mean flow defect is detected. As Re_Q increases for fixed $\mathrm{Re}_\theta=100$, the final amplitude of the unstable spiral perturbations grows more and more. For the next case reported here ($\mathrm{Re}_Q=200$), the amplitude is already so large that a significant mean flow defect is detected: after the nominal flow rate $\mathrm{Re}_Q=200$ is reached, the instability of the RHPF produces spiral nonlinear waves that consume part of the energy due to the pressure difference put into the flow and the mean flow rate decreases. But these nonlinear waves still correspond to convective instabilities, so that the mean flow rate oscillates in time as a consequence of the passing of the successive wavetrains through the pipe.

These traveling waves solutions also coincide with the

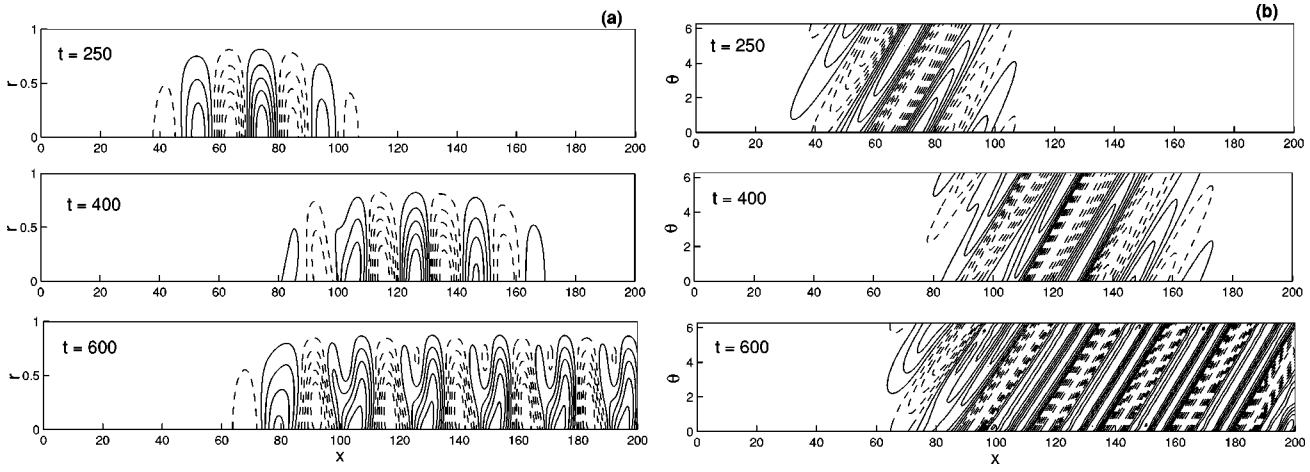

FIG. 18. Contour lines of the radial velocity u at $\theta=0$ on the rx-plane (a), and for $r=1/2$ on the θx plane (b), for different times (as indicated) in the case $\mathrm{Re}_Q=200$ and $\mathrm{Re}_\theta=300$. Continuous (dashed) lines correspond to positive (negative) values of u. Nine positive and nine negative equidistant contour lines of u are plotted in the following intervals: (a) $[-2\times10^{-6},2\times10^{-6}]$ for $t=250$, $[-0.03,0.03]$ for $t=400$, and $[-0.07,0.064]$ for $t=600$; (b) $[-1.12\times10^{-6},1.15\times10^{-6}]$ for $t=250$, $[-0.017,0.017]$ for $t=400$, and $[-0.051,0.044]$ for $t=600$.

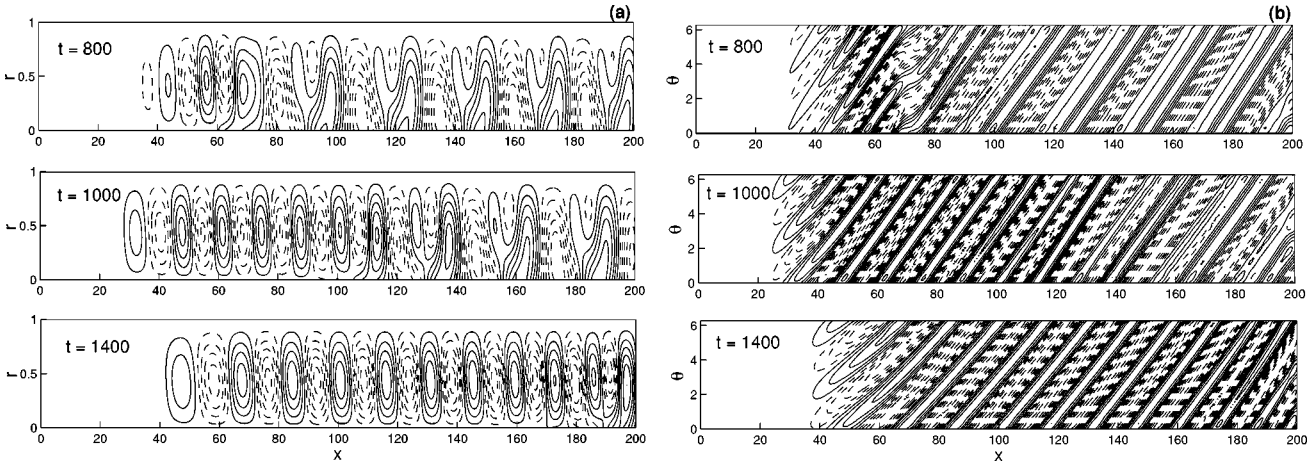

FIG. 19. As in Fig. 18, but for different times (as indicated). The range of values of u plotted are the following: (a) $[-0.066, 0.065]$ for $t=800$, $[-0.061, 0.055]$ for $t=1000$, and $[-0.045, 0.051]$ for $t=1400$; (b) $[-0.054, 0.054]$ for $t=800$, $[-0.047, 0.048]$ for $t=1000$, and $[-0.047, 0.051]$ for $t=1400$.

ones found by Toplosky and Akylas for an infinite pipe.[5] These authors looked for 2D, periodic spiral wave solutions of the governing equations for the pressure driven flow in an infinite rotating pipe and found that these solutions bifurcate supercritically from RHPF at Mackrodt's linear-neutral-stability curve for convective instabilities (see Fig. 1), so that they are equivalent to the traveling waves found here in a long rotating pipe. According to Barnes and Kerswell,[6] these 2D helical waves may become 3D helical waves by a secondary instability. The neutral curve for this secondary instability lies on the Re_Q-Re_θ plane between Mackrodt's neutral curve for convective instabilities and the neutral curve for the onset of absolute instabilities (see Fig. 2 in Ref. 6 and compare it with Fig. 1 above). Actually, the case considered in Sec. III B is within this secondary instability region, though the case considered in Sec. III C is not. However, since these 3D helical traveling waves are characterized by a slow variation of the axial wavelength along the axis of the pipe, they are very difficult to detect numerically in a finite pipe.

The next numerical experiments are intended to investigate the nature of the flow when the linear stability analysis predicts an absolute instability. Thus, for a fixed pressure difference, which corresponds to a nominal axial Reynolds number $\mathrm{Re}_Q=200$, we increase the rotation rate of the pipe. Just above the neutral curve for the onset of absolute instability ($\mathrm{Re}_\theta=300$), we observe a complicate temporal evolution of the flow. After the nominal axial flow rate is reached, different spiral *traveling* waves arise from convective instabilities, thus propagating downstream. Eventually, some of these wave packets begin to travel upstream also, until a final steady state which consists on a *standing* spiral wave superimposed to the RHPF is set throughout the pipe. For a higher rotation rate ($\mathrm{Re}_\theta=400$), the transition from a traveling wave to a standing wave is more straightforward, and the final standing spiral wave corresponds to an azimuthal wave number $n=-2$. In both cases, the mean flow defect is quite significant (close to 20% in the last case), and remains constant in time once the standing wave is developed. The transition

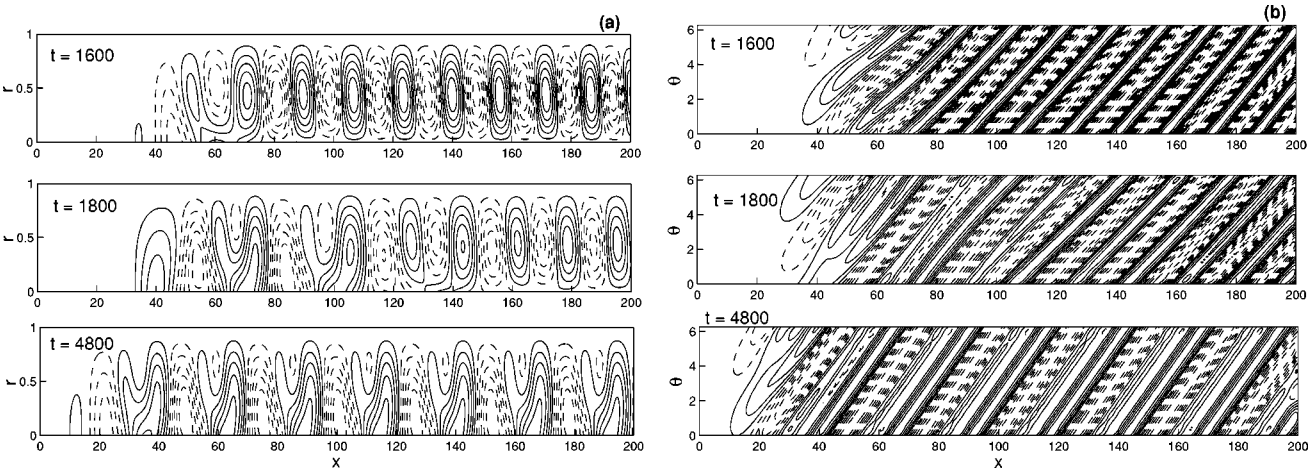

FIG. 20. As in Fig. 18, but for different times (as indicated). The range of values of u plotted are the following: (a) $[-0.044, 0.041]$ for $t=1600$, $[-0.058, 0.052]$ for $t=1800$, and $[-0.063, 0.057]$ for $t=4800$; (b) $[-0.044, 0.042]$ for $t=1600$, $[-0.046, 0.045]$ for $t=1800$, and $[-0.048, 0.042]$ for $t=4800$.

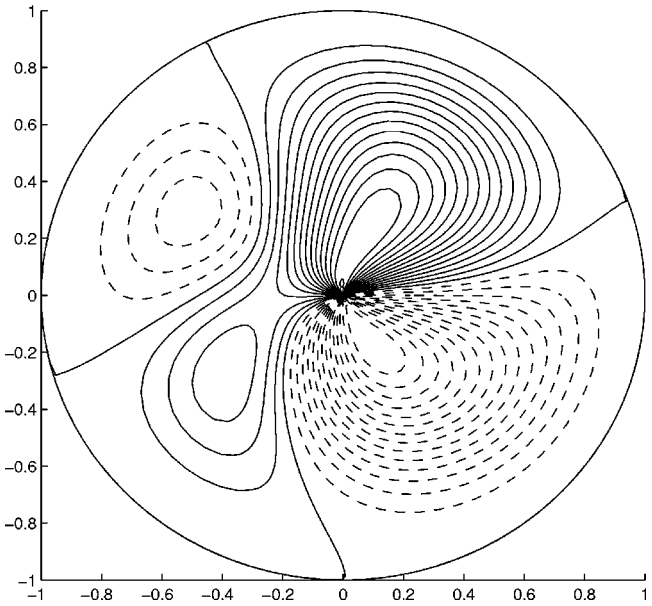

FIG. 21. Contour lines of the radial velocity u on the θr-plane at the pipe exit ($x=200$) and $t=4800$ for $\mathrm{Re}_Q=200$ and $\mathrm{Re}_\theta=300$. Continuous (dashed) lines correspond to positive (negative) values of u (15 positive and 15 negative equidistant values of u are plotted in the interval $[-0.047, 0.044]$).

from a traveling spiral wave to a standing spiral wave when RHPF goes from convectively unstable to absolutely unstable is the main finding of this work.

ACKNOWLEDGMENTS

This work was supported by the Ministerio de Educación y Ciencia of Spain (Grant No. FIS04-00538). All the numerical computations have been made in the computer facilities at the SAIT (U.P. Cartagena).

APPENDIX: NUMERICAL METHOD

In this appendix we summarize the numerical technique used in this work,[9] including the improvements incorporated here, and give some numerical details of the simulations. The

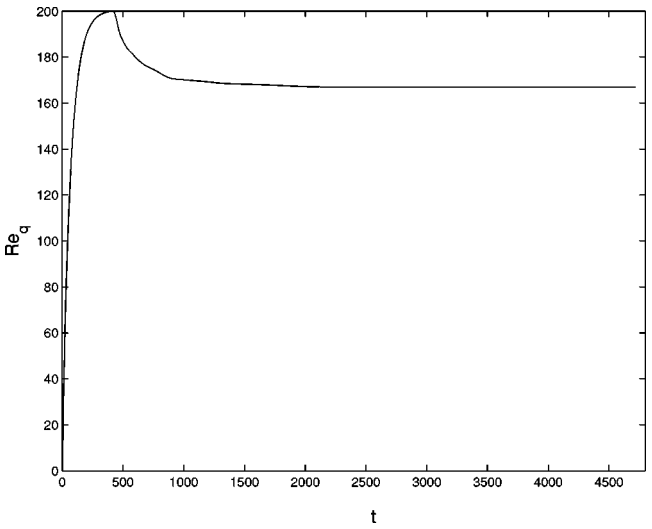

FIG. 22. $\mathrm{Re}_q(t)$ for $\mathrm{Re}_Q=200$ and $\mathrm{Re}_\theta=400$.

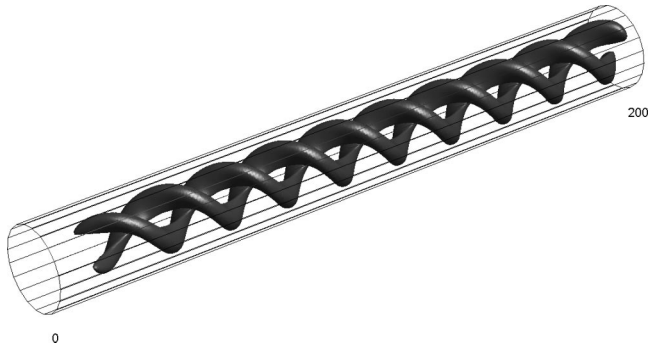

FIG. 23. 3D view of the isosurface $u=0.02$ for $t=4800$ in the case $\mathrm{Re}_Q=200$ and $\mathrm{Re}_\theta=400$.

accuracy of the numerical method for the present problem has also been checked in Ref. 9. For instance, Fig. 9 of that reference compares the temporal evolution of the azimuthal velocity component obtained numerically for $\mathrm{Re}_Q=100$ and $\mathrm{Re}_\theta=30$ (a stable case) with an analytical solution.

To solve Eqs. (1) and (2) we use a projection method (see, e.g., Ref. 11, for a recent account): at each time step $t^n=t^{n-1}+\Delta t$, an intermediate velocity field $\mathbf{v}^*$ that does not satisfy the divergence constraint (1) is first obtained from (2) with vanishing pressure gradient; then, the pressure is obtained from a Poisson equation that comes from the incompressibility constraint,

$$\nabla^2 p = \frac{1}{\Delta t}\,\boldsymbol{\nabla}\cdot\mathbf{v}^* . \tag{A1}$$

The particularity of the method given in Ref. 9 is that a technique is developed to solve Eq. (A1) with Dirichlet boundary conditions for the pressure on part of the inlet and outlet sections of the pipe, which warrants the incompress-

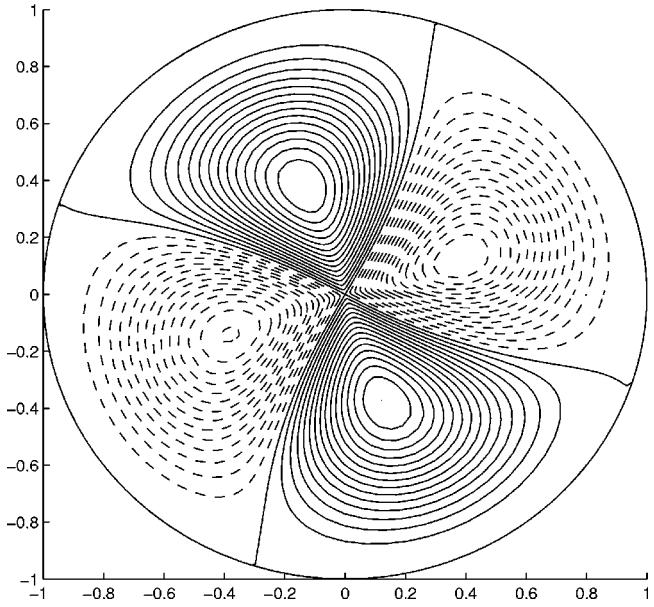

FIG. 24. Contour lines of the radial velocity u on the θr plane at the pipe exit ($x=200$) and $t=4800$ for $\mathrm{Re}_Q=200$ and $\mathrm{Re}_\theta=400$. Continuous (dashed) lines correspond to positive (negative) values of u (15 positive and 15 negative equidistant values of u are plotted in the interval $[-0.036, 0.034]$).

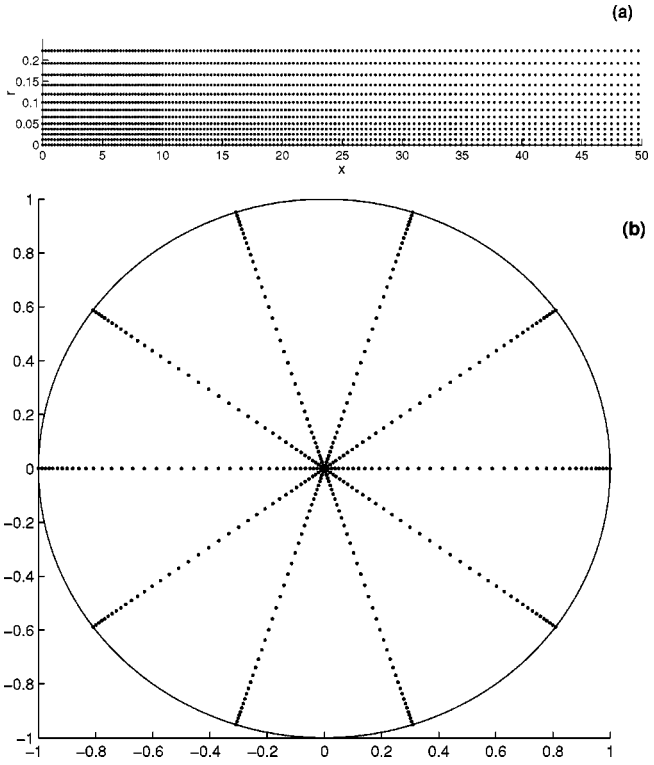

FIG. 25. Detail of the nonuniform grid used in the computations on the rx plane (a) and on the $r\theta$-plane (b).

ibility constraint, and leaves the flow to evolve freely in time on these surfaces. To that end, one solves

$$\nabla_\tau \cdot \nabla_\tau p = \frac{1}{\Delta t} \nabla_\tau \cdot \mathbf{v}_\tau^* \tag{A2}$$

on the inlet and outlet surfaces, at $x=0$ and $x=l$, respectively, where ∇_τ is the part of the ∇ operator with derivatives on the surface normal to the axis and $\mathbf{v}_\tau^*=(u^*,v^*)$. This equation is solved in Ref. 9 with $p=1$ on the curve $r=1$ for $x=0$ and $p=0$ on the curve $r=1$ for $x=l$. Here we propose to give more liberty to the inflow and the outflow conditions by fixing p just at one point ($r=0$) on each one of these surfaces. In fact, we solve (A2) with the Neumann boundary condition $\partial p/\partial r = u^*/\Delta t$ at the wall contour $r=1$. The resulting undetermined problem is solved using a successive over-relaxation scheme.[12] At each time step we use the previous time solution as seed and a relaxation parameter value of 1.275. Then, the solution at the inlet ($x=0$) is fixed by adjusting $p=1$ at $r=0$ and the solution at the outlet ($x=l$) by adjusting $p=0$ at $r=0$.

In order to simplify the treatment of the singularity of the (cylindrical) equations at the axis, we actually solve numerically Eqs. (1) and (2) with the dependent variable $r\mathbf{v}$ instead of $\mathbf{v}$. We use a nonuniform spatial grid of $(n_r=39)\times(n_\theta=10)\times(n_x=431)$ nodes and $\Delta t=2\times10^{-3}$. Some details of the nonuniform grid are plotted in Fig. 25. Second order accuracy in time is reached by using a predictor-corrector scheme at each time step. Second order accuracy is also used for the derivatives in the radial (r) and axial (x) directions, while for the angular coordinate θ we use an eighth order accuracy scheme. To circumvent the memory limitations of our computer facilities, a second order ADI technique is used to solve the discretized Poisson equation for the pressure (A1) at each time step. This requires an initial guess for the pressure distribution at $t=0$, which for an initial fluid at rest is simply a linear function of x between 1 and 0. A typical simulation occupies 140 Mbytes of random access memory, and takes about 180 h of CPU in a Compaq HPC160 processor.

[1] T. J. Pedley, "On the instability of viscous flow in a rapidly rotating pipe," J. Fluid Mech. **35**, 97 (1969).
[2] P. A. Mackrodt, "Stability of Hagen–Poiseuille flow with superimposed rigid rotation," J. Fluid Mech. **73**, 153 (1976).
[3] F. W. Cotton and H. Salwen, "Linear stability of rotating Hagen–Poiseuille flow," J. Fluid Mech. **108**, 101 (1981).
[4] R. Fernandez-Feria and C. del Pino, "The onset of absolute instability of rotating Hagen–Poiseuille flow: A spatial stability analysis," Phys. Fluids **14**, 3087 (2002).
[5] N. Toplosky and T. R. Akylas, "Nonlinear spiral waves in rotating pipe flow," J. Fluid Mech. **190**, 39 (1988).
[6] D. R. Barnes and R. R. Kerswell, "New results in rotating Hagen–Poiseuille flow," J. Fluid Mech. **417**, 103 (2000).
[7] T. Loiseleux, I. Delbende, and P. Huerre, "Absolute and convective instabilities of a swirling jet/wake shear layer," Phys. Fluids **12**, 375 (2000).
[8] C. Olendraru and A. Sellier, "Viscous effects in the absolute-convective instability of the Batchelor vortex," J. Fluid Mech. **459**, 371 (2002).
[9] R. Fernandez-Feria and E. Sanmiguel-Rojas, "An explicit projection method for solving incompressible flows driven by a pressure difference," Comput. Fluids **33**, 463 (2004).
[10] G. K. Batchelor and A. E. Gill, "Analysis of the stability of axisymmetric jets," J. Fluid Mech. **14**, 529 (1962).
[11] D. L. Brown, R. Cortez, and M. L. Minion, "Accurate projection methods for the incompressible Navier–Stokes equations," J. Comput. Phys. **168**, 464 (2001).
[12] R. L. Burden and J. D. Faires, *Numerical Analysis* (PWS-Kent, Boston, 1993).